PCCP

ROYAL SOCIETY OF CHEMISTRY

PAPER

View Article Online
View Journal | View Issue

Cite this: *Phys. Chem. Chem. Phys.*, 2024, **26**, 5704

Towards understanding the lower CH_4 selectivity of HCP-Co than FCC-Co in Fischer–Tropsch synthesis†

Dan Luo,[ab] Xingchen Liu, *[bc] Tong Chang,[a] Jiawei Bai,[b] Wenping Guo,[d] Wentao Zheng[b] and Xiaodong Wen *[bcd]

Received 12th December 2023,
Accepted 16th January 2024

DOI: 10.1039/d3cp06041a

rsc.li/pccp

In Fischer–Tropsch synthesis (FTS), the cobalt catalyst has higher C_{5+} and lower CH_4 selectivity in the hcp phase than in the fcc phase. However, a detailed explanation of the intrinsic mechanism is still missing. The underlying reason was explored combining density functional theory, Wulff construction, and a particle-level descriptor based on the slab model of surfaces that are prevalent in the Wulff shape to provide single-particle level understanding. Using a particle-level indicator of the reaction rates, we have shown that it is more difficult to form CH_4 on hcp-Co than on fcc-Co, due to the larger effective barrier difference of CH_4 formation and C–C coupling on hcp-Co particles, which leads to the lower CH_4 selectivity of hcp-Co in FTS. Among the exposed facets of fcc-Co, the (311) surface plays a pivotal role in promoting CH_4 formation. The reduction of CH_4 selectivity in cobalt-based FTS is achievable through phase engineering of Co from fcc to hcp or by tuning the temperature and size of the particles.

1. Introduction

The ultimate goal for catalysis study is to design catalysts with high stability, activity, and selectivity. Although the design principles for catalysts of high stability and activity have been well-established,[1,2] it remains a substantial challenge to understand the relationship between the structure of a catalyst and its selectivity, especially for reactions with complex product distributions. A typical example for which selectivity is intricate is Fischer–Tropsch synthesis (FTS), which converts the simple mixture of CO and H_2 (syngas) to a broad spectrum of chemicals (C_1–C_{70+}), including methane, paraffins, olefins, and different oxygenated species such as aldehydes, ketones, acids, and alcohols.[3] Co-based catalysts are widely used in the low-temperature FTS process, due to their high activity, relatively high selectivity to long-chain paraffins, and low water–gas shift side reactions.[4–7] Still, in the FTS process, methanation is the main competing pathway for chain growth.[8–10] To date, a great deal of effort has been devoted to controlling the product distribution of FTS by changing the catalyst formulations.[11–15]

It is generally accepted that the catalytic performances of inorganic solids can be tuned by their composition,[11,16] crystallographic structure (phase),[17,18] size,[19,20] shape,[21] chelating molecular ligands,[22,23] and support.[24] Among these factors, the crystalline phase lies at the heart of the structural parameters for solids of given composition. It determines how the constituents (atoms or ions) are arranged in a highly ordered microscopic structure, and governs the electronic structures and surface atomic geometry of catalysts.[18,25] Besides the most stable phase, the various metastable phases of the catalysts can usually be stabilized by the reactive gas/liquid and often high-temperature environments,[26–29] which makes it possible to modulate the catalytic performances of materials by phase engineering.

Chen *et al.*[30] found that the 4H Cu and 4H/fcc Cu shells exhibit greater CO_2 reduction reaction activity and better C_2H_4 selectivity compared to fcc Cu, demonstrating the crystal phase-dependent C_2H_4 selectivity of Cu. Alumina with different crystal phases shows that CoMo/θ-Al_2O_3 has a much higher hydrodesulfurization selectivity than CoMo/γ-Al_2O_3 and CoMo/δ-Al_2O_3.[31] The sorption and catalytic behavior observed between the alkaline ferrites studied are associated with the crystal structures and alkali composition.[32] In FTS, Gnanamani *et al.*[33] used a different catalyst reduction process to obtain

[a] *Shanxi Key Laboratory of Ecological Protection and Resources Utilization of Yuncheng Salt Lake, Department of Applied Chemistry, Yuncheng University, 1155 Fudan West Street, Yuncheng 044000, China*
[b] *State Key Laboratory of Coal Conversion, Institute of Coal Chemistry, Chinese Academy of Sciences, Taiyuan, 030001, China. E-mail: liuxingchen@sxicc.ac.cn, wxd@sxicc.ac.cn*
[c] *University of Chinese Academy of Sciences, No. 19A Yuquan Road, Beijing, 100049, P. R. China*
[d] *National Energy Center for Coal to Liquids, Synfuels China Co., Ltd, Huairou District, Beijing, 101400, China*

† Electronic supplementary information (ESI) available: Detailed data about the CH_4 formation and C_1 + C_1 coupling on hcp-Co and fcc-Co surfaces. See DOI: https://doi.org/10.1039/d3cp06041a

distinct phases of cobalt, and found that the hcp phase shows higher CO conversion and lower CH_4 selectivity than the fcc phase. Du *et al.*[34] found that the multistep activation process derived catalyst (CoZr/AC-RSCR) with more hcp phase has higher CO conversion and lower CH_4 selectivity than the H_2 reduction derived catalyst (CoZr/AC-R) with more fcc phase.

However, despite the extensive experimental observations of phase-dependent product selectivity of catalysts, the connection between the crystalline phase of a catalyst and its product selectivity remains obscure. A major obstacle in experiments is that the catalyst particles with known crystal phases are composed of multiple facets, due to which their identity and functioning mechanism may be different. It has been proposed by Zhong *et al.* that different crystal phases have different surface reactivities because of the distinct intrinsic surface strains.[35] It has been demonstrated that the isolated Pd sites on the surfaces of the particles determine the high selectivity in acetylene semi-hydrogenation reaction for intermetallic Pd-X (X = Ga or In) materials with multiple phases.[36] Several theoretical studies on the CH_4 selectivity of Fe_5C_2 surfaces also showed that the selectivity is highly facet dependent.[37,38]

In FTS reactions, the selectivity of products is mainly determined by the competition of the coupling between C + H and C + C.[39,40] Due to the interrelated nature of all individual selectivities indicated by the linear relationship between the individual C_1–C_4 hydrocarbon selectivities and the C_{5+} selectivity,[8–10] CH_4 selectivity can be used as an indicator of the product selectivity in FTS.[41,42] Hydrogenation of carbon species, which is produced through CO dissociation, is the major pathway to CH_4 formation, and it has been well accepted that $CH_3 + H \rightarrow CH_4$ is the rate-determining step.[38,41,43] Previously, the CH_4 selectivity of a few intuitively selected Co surfaces has been studied, such as the (100), (110), (111) and (311) of fcc-Co by Yu *et al.*[44] and the (0001) of hcp-Co by Cheng *et al.*[45] However, as the overall CH_4 selectivity of a Co particle is contributed by all its exposed facets, the fundamental cause for the lower CH_4 selectivity of hcp-Co than fcc-Co remains elusive.

In this work, we propose to use a theoretical approach to investigate the correlation between the crystalline phases of Co (hcp and fcc) and their CH_4 selectivity at the single particle level using the slab model of surfaces that are prevalent in the Wulff shape. CH_4 selectivity of hcp-Co and fcc-Co was evaluated by considering the competition between CH_4 formation and $C_1 + C_1$ coupling on all the prominent surfaces that covers the exterior of particles based on the Wulff theorem. The facet dependent effective barriers for CH_4 selectivity were then integrated into a particle-level energy descriptor[46] and compared between hcp and fcc Co. Finally, the conditions for phase transition between hcp and fcc were explored with respect to temperature and nanoparticle size to obtain catalysts with higher performances. We envision that our proposed strategy can effectively scoop out the selectivity information of probe reactions occurring on each facet and thereby reasonably add-up these results to represent those of the single particle level. As such, this approach allows us to understand the difference in the intrinsic selectivity of particles with different crystalline phases. We anticipate that this simplified strategy not only can lessen the gap between theoretical methodology and experimental understanding in cobalt-catalyzed FTS study, but may also be applicable to other catalysis systems to understand the correlation between the crystal phase and product selectivity.

2. Methods and models

2.1 Computational details

All DFT calculations were performed using the Vienna Ab Initio simulation package (VASP).[47,48] The electron–ion interaction was described with the projector augmented wave (PAW) method.[49,50] The electron exchange and correlation energies were treated within the generalized gradient approximation in the Perdew–Burke–Ernzerhof formalism (GGA-PBE).[51] The different cutoff energies are given in Tables S1 and S2 (ESI†); according to the energy and lattice constant of bulk cobalt, the cutoff of plane wave basis set was set up to 450 eV. The Monkhorst–Pack *k*-point sampling was used. Electron smearing was employed according to the Methfessel–Paxton[52] technique, with a smearing width σ = 0.2 eV. Due to the large influence of magnetic properties on the adsorption energies, spin polarization was taken into consideration. To locate transition states, we used the Nudged Elastic Band (NEB) method.[53] A vibrational frequency analysis was performed to verify whether a transition state is associated with a single imaginary frequency.

2.2 Model

Slab models of surfaces that are prevalent in the Wulff shapes were utilized as proxies of the cobalt particles. For the hcp-Co and fcc-Co surfaces, the optimized lattice constants of hcp-Co ($a = b$ = 2.49 Å and c = 4.03 Å) with a 13 × 13 × 7 *k*-point agree well with the experimental ($a = b$ = 2.51 Å, c = 4.06 Å)[54] and calculated ($a = b$ = 2.49 Å, c = 4.03 Å)[55] values, which are given in Table S1 (ESI†). The optimized lattice constants of fcc-Co ($a = b = c$ = 3.52 Å) with a 13 × 13 × 13 *k*-point also agree with the experimental ($a = b = c$ = 3.54 Å)[56] and the calculated ($a = b = c$ = 3.52 Å)[57] values, which are given in Table S2 (ESI†). We adopted the equilibrium shape of the hcp-Co and fcc-Co particles using Wulff construction at *ab initio* accuracy reported in the previous work (Fig. 1 and Table S3, ESI†).[18] The hcp-Co particles are predicted to be covered by surfaces of (10−11), (10−10), (0001), (10−12), (11−20), and (11−21), while the fcc-Co particles are covered by the surfaces of (111), (100), (311), and (110). We choose unit cells $p(4 \times 4)$ for hcp-Co (0001), (11−21), fcc-Co (100), and (111), and $p(4 \times 2)$ unit cells for hcp-Co (10−10), (10−11), (10−12), (11−20) and fcc-Co (110), (311), as shown in Fig. 1 and Fig. S1 (ESI†). A 3 × 3 × 1 *k*-point sampling was used for all surfaces. The atoms in the top two layers of the slab models for hcp-Co and fcc-Co are fully allowed to relax while the bottom two layers atoms are fixed.

2.3 The adsorption energy and reaction barrier

The adsorption energy of C-containing species on cobalt surfaces was calculated according to the equation

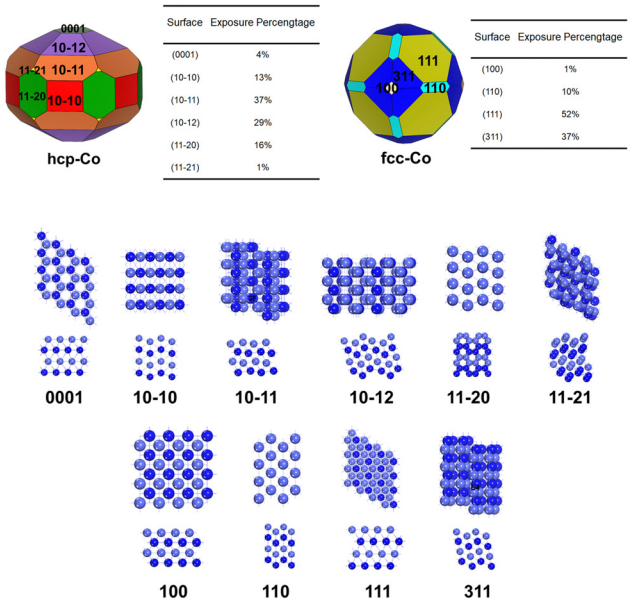

Fig. 1 Wulff construction and the utilized slab models of the prevalent surfaces of hcp-Co and fcc-Co in the Wulff shapes.

$$E_{ads} = E_{slab/X} - E_{slab} - E_X, \quad (1)$$

where $E_{slab/X}$ is the total energy of the slab with the adsorbates. X is equilibrium geometry, E_{slab} is the energy of the clean surface, and E_X is the energy of the free adsorbate X in the gas phase.

The reaction barrier E_a and the reaction energy E_r were calculated according to the equations:

$$E_a = E_{TS} - E_{IS} \quad (2)$$

$$E_r = E_{FS} - E_{IS} \quad (3)$$

where E_{IS}, E_{TS} and E_{FS} are energies of the corresponding initial (IS), transition (TS), and final (FS) states, respectively. We used the zero point energy (ZPE) to correct all energies.

To estimate the relative activity of reactions on the particles of different Co phases, we use the concept of particle effective barrier which is a particle-level indicator of the reaction activity defined previously in the literature.[45] The particle effective barriers for CH_4 formation ($E_{a\_particle,CH_4}$) and the most feasible $C_1 + C_1$ coupling ($E_{a\_particle,C_1+C_1}$) and the difference of them ($\Delta E_{a\_particle}$) were calculated in terms of rates as follows. First, we assume that the overall reaction rate (r) is the sum of the contributions from all the exposed surfaces. This assumption is valid as it has been recently proven unambiguously that in Co-catalyzed FTS reactions, the edges and vertices of the particles are responsible for the CO dissociation, while the C–C and C–H coupling reactions happen mainly on the flat surfaces of the catalyst particles.[58,59]

Based on the Arrhenius formula, the reaction rate r on a particle with i surfaces can be calculated according to the equation[46,60]

$$r = \sum_i r_i = \sum_i (k_i S_i m_i) = \sum_i \left(A_i e^{\frac{-E_{a,i}}{RT}} S_i m_i \right) = A e^{\frac{-E_{a\_particle}}{RT}} Sm \quad (4)$$

where r_i, k_i, S_i, A_i and $E_{a,i}$ are the reaction rate, rate constant, surface area, number of sites per unit area, pre-exponential factor and reaction barrier on the i_{th} surface. A, S, m are the pre-exponential factor, surface area, and the number of sites per unit area, respectively, on hcp-Co and fcc-Co surfaces. We assume that m_i and A_i on different surfaces are the same and equal to the values on hcp-Co and fcc-Co surfaces and defined as the exposed relative ratio of surface i, which is equal to S_i/S. Thus, the effective barrier of the reaction on the particle $E_{a\_particle}$ can be calculated according to the equation

$$E_{a\_particle} = -RT \ln \left[\sum_i \left(e^{\frac{-E_{a,i}}{RT}} S_{S,i} \right) \right] \quad (5)$$

2.4 Phase transition calculation

To obtain the conditions of phase transition between hcp and fcc, the influence of temperature and size on the Gibbs free energy (G) of bulk Co phases was considered. The Gibbs free energy for the solid phase particle is defined as the summation of the Gibbs free energy in the bulk and the surface.[61,62] The Gibbs free energy of bulk hcp-Co and fcc-Co was calculated according to the equation in the literature[63,64]

$$G = E^{DFT} + E^{vib} + E^{surf} \quad (6)$$

where E^{DFT} is the energy per cobalt atom of hcp-Co or fcc-Co. E^{vib} is the phonon energy per cobalt atom of hcp-Co or fcc-Co at different temperatures. The phonon energies are calculated by using the PHONON software.[65] E^{surf} is the surface energy per cobalt atom of hcp-Co or fcc-Co at different sizes of cobalt nanoparticles. For simplicity, we assume the cobalt nanoparticles to be spherical of different sizes, and the surface energy[66] is calculated according to

$$E^{surf} = \gamma_m A_m \quad (7)$$

where γ_m is the surface energy per unit surface area of hcp-Co or fcc-Co; A_m is the molar surface area:

$$A_m = \frac{MA}{\rho V} \quad (8)$$

Here, M is the molar mass of hcp-Co or fcc-Co, A is the spherical surface area, ρ is the density of hcp-Co or fcc-Co, and V is the spherical volume.

3. Results and discussion

3.1 CH_4 formation

We first study the elementary steps of CH_4 formation on cobalt surfaces: C + H → CH, CH + H → CH_2, CH_2 + H → CH_3, and CH_3 + H → CH_4. The methanation potential energy surfaces are given in Fig. 2. The structures of the initial state (IS), transition state (TS), and final state (FS) for the elementary steps are provided in Fig. S1 and S2 (ESI†) and the reaction barriers and reaction energies of hcp-Co and fcc-Co are listed in Tables S4–S6 (ESI†). As shown in Fig. 2, the total energy of the TS has an increasing tendency along the hydrogenation reaction

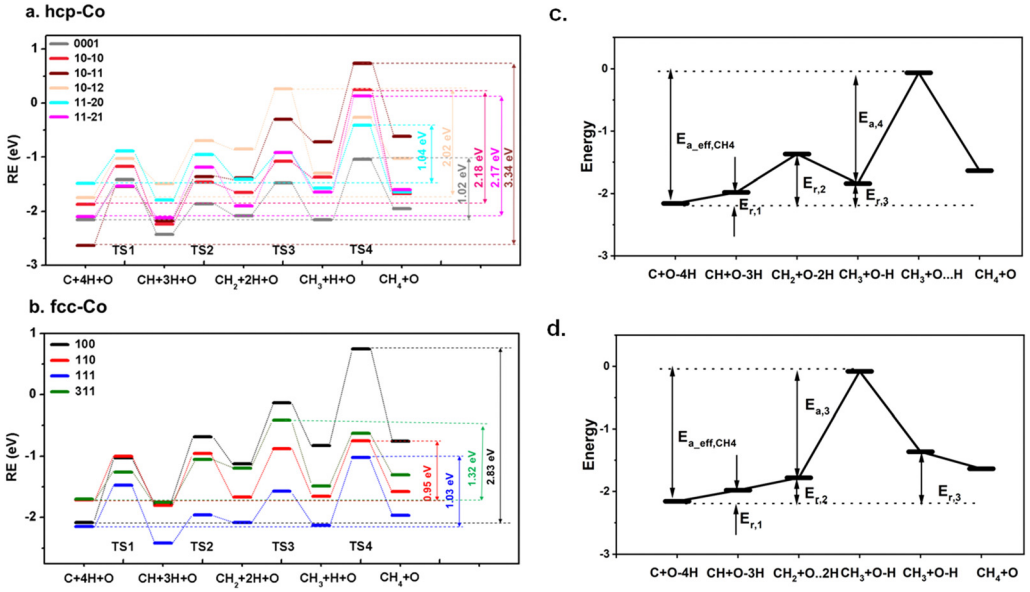

Fig. 2 Methanation potential energy surface for C(g) + $2H_2$(g) + O → CH_4(g) + O on cobalt surfaces (a) hcp-Co; (b) fcc-Co (relative energy (RE) is the adsorption energy of 4H atoms on cobalt surfaces). Schematic illustration of the effective barrier to CH_4 formation (E_{a_eff,CH_4}) (c) hcp-Co (0001), (10−10), (10−11), (11−20), (11−21), fcc-Co (100), (110), (111); (d) hcp-Co (10−12) and fcc-Co (311).

coordinate on most hcp-Co and fcc-Co surfaces, and the addition of the fourth hydrogen is usually the rate-limiting step, which is consistent with previous studies.[42,55,67] The increase of the reaction barrier illustrates that C hydrogenation becomes more and more difficult on cobalt surfaces to form CH_4. But on (10−12) and (311), the step with the highest barrier is CH_2 hydrogenation, which is different from the result of Qin *et al.*[68] and Yu *et al.*[44] This is likely due to the absence of zero point energy corrections in these studies.

Following the approach of Cheng,[42,69] the effective barriers of CH_4 formation (E_{a_eff,CH_4}) were used to evaluate the catalytic activity of the Co surfaces to produce CH_4. As CH_4 formation happens by stepwise C hydrogenation, the rate-determining step is (CH_3 + H → CH_4) on most of the Co surfaces. Before the rate-determining step, the preceding hydrogenation steps may reach quasi-equilibrium. Thus, the rate of CH_4 formation can be calculated as the rate of the rate-liming step:

$$r_{CH_4} = A\exp[-E_{a,4}/RT]\theta_{CH_3}\theta_H = A\exp[-(E_{a,4} + E_{r,3})/RT](\theta_C\theta_*)^3\theta_C\theta_H \quad (9)$$

Here, A is the pre-exponential factor. θ_{CH_3}, θ_C, θ_H, and θ_* are the coverage of CH_3, C, H, and the free site on the surface, respectively. R is the ideal gas constant and T is the reaction temperature. $E_{a,4}$ is the reaction barrier of CH_3 hydrogenation, and $E_{r,3}$ is the reaction energy for C + 3H → CH_3. From eqn (10), it is evident that the effective barrier of CH_4 formation (E_{a_eff,CH_4}) can be calculated as ($E_{a,4} + E_{r,3}$), which is essentially the difference between the highest TS energy of CH_4 formation (E_{TS_4}) and the initial state with one atomic carbon, one atomic oxygen and four atomic hydrogens adsorbed on cobalt surfaces (E_{C+4H+O})[38,41,42] (Fig. 2c).

$$E_{a\_eff,CH_4} = E_{a,4} + E_{r,3} = E_{TS_4} - E_{C+4H+O} \quad (10)$$

However, the difference between the barrier from CH_3 + H + O toward TS_3 is higher than that toward TS_4 by 0.53 eV on hcp-Co (10−12), and 0.21 eV on fcc-Co (311), respectively. Since the ratio of hydrogen to the free site coverage θ_H/θ_* is about 1 to 10 under typical reaction conditions (assuming equivalent coverages of H and free site *), the higher barrier of CH_3 + * → CH_2 + H than CH_3 + H → CH_4 causes $r_{-3} = k_{-3}\theta_{CH_3}\theta_* \ll r_4 = k_4\theta_{CH_3}\theta_H$. Thus, the reaction of CH_2 + H → CH_3 is irreversible and becomes the rate-determining step on (10−12) and (311), and the rate of CH_4 formation on these two surfaces should be calculated as:

$$R_{CH_4} = A\exp[-E_{a,3}/RT]\theta_{CH_2}\theta_H = A\exp[-(E_{a,3} + E_{r,2})/RT](\theta_H/\theta_*)^2\theta_C\theta_H \quad (11)$$

The effective barrier of CH_4 formation (E_{a_eff,CH_4}) on (10−12) and (311) surfaces therefore is determined as the difference between the highest TS energy of CH_4 formation (E_{TS_3}) and the initial state (E_{C+4H+O}) (Fig. 2d).

$$E_{a\_eff,CH_4} = E_{a,3} + E_{r,2} = E_{TS_3} - E_{C+4H+O} \quad (12)$$

To assess the activity of the Co surfaces for CH_4 formation, the E_{a_eff,CH_4} values for all the studied surfaces of hcp and fcc Co are obtained and are plotted in Fig. 3(a). Surprisingly, the CH_4 formation activity on hcp is not always lower than that on fcc. The E_{a_eff,CH_4} of fcc-Co (110), which is the lowest one on fcc-Co, is slightly smaller than that of hcp-Co (0001) and hcp-Co (11−20). The rank of effective barriers is hcp-Co (10−11) > fcc-Co (100) > hcp-Co (10−10) > hcp-Co (11−21) > hcp-Co (10−12) > fcc-Co (311) > hcp-Co (11−20) ≈ fcc-Co (111) ≈ hcp-Co (0001) ≈ fcc-Co (110). It shows that hcp-(0001), hcp-(11−20), fcc-(111) and fcc(110) are all active and have similar catalytic activities in CH_4 formation. The rank of the effective

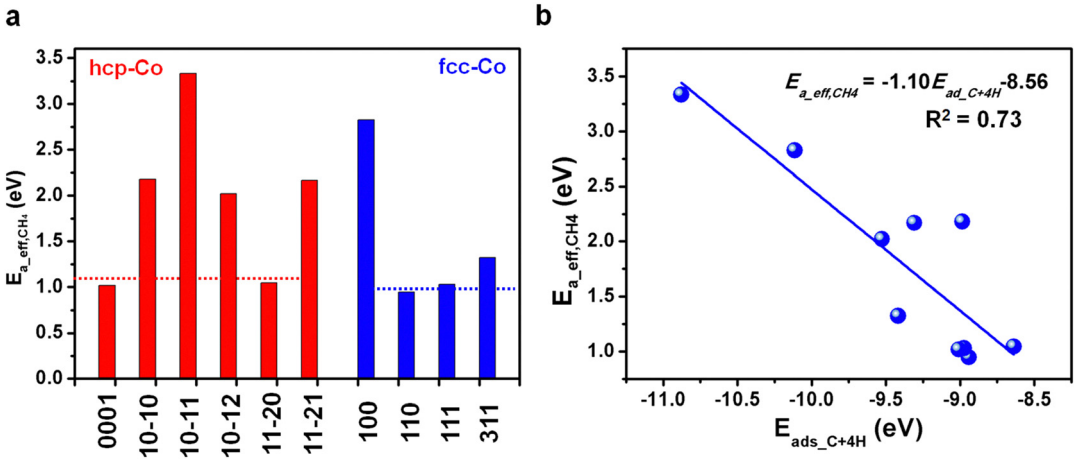

Fig. 3 (a) The effective barriers of CH_4 formation (E_{a_eff,CH_4}) on hcp-Co and fcc-Co surfaces and the average effective barrier of CH_4 formation ($E_{a\_particle,CH_4}$) for Co particles (dashed lines). (b) E_{a_eff,CH_4} as a function of the sum of adsorption energies of C + 4H atoms (E_{ads_C+4H}) of each cobalt surface.

barrier for CH_4 formation is consistent with previous *ab initio* studies.[44,66]

To assess the overall catalytic activity of hcp-Co and fcc-Co phases for CH_4 formation, we further calculated the particle effective barriers ($E_{a\_particle,CH_4}$) of CH_4 formation on hcp-Co and fcc-Co Wulff particles, assuming that the overall rate of reaction on the catalyst particle is the sum of the rates from all its exposed surfaces (see the Methods section). On hcp-Co, $E_{a\_particle,CH_4}$ is 1.11 eV and on fcc-Co it is 1.02 eV (Fig. 3(a) and Table S7, ESI†). The results indicate that hcp-Co and fcc-Co have similar intrinsic catalytic activity to form CH_4.

A weak linear relationship was discovered between E_{a_eff,CH_4} of the Co surface and the sum of adsorption energies of a C atom and 4 H atoms on it (E_{ads_C+4H}) with R^2 of 0.73 on ten surfaces, irrespective of the crystal phase (Fig. 3(b) and Table S8, ESI†). With the adsorption of C and 4 H atoms becoming stronger, the acquired E_{a_eff,CH_4} follows a downhill trend on the cobalt surfaces, and the higher values of E_{ads_C+4H} are associated with lower E_{a_eff,CH_4}. This linear correlation allows the fast estimation of the effective barrier of CH_4 formation on cobalt surfaces, as long as the adsorption energies of C and H are given ($E_{a\_eff,CH_4} = -1.10E_{ad\_C+4H} - 8.56$).

3.2 $C_1 + C_1$ coupling

The carbon chain elongation process in FTS was investigated through the carbide mechanism[70] ($CH_i + CH_j \rightarrow CH_iCH_j$, i, j = 0–3) and CO-insertion mechanism[71] ($CH_i + CO \rightarrow CH_iCO$, i = 0–3). The structures of the $C_1 + C_1$ coupling for IS, TS, FS are shown in Fig. S3–S12 (ESI†), and the reaction barriers and energies are given in Tables S5 and S6 (ESI†).

In the carbide mechanism, the $CH_i + CH_j$ coupling rate is expressed as:

$$r_{CH_i+CH_j} = A\exp[-E_{a,i+j}/RT]\theta_{CH_i}\theta_{CH_j} = A\exp[-(E_{a,i+j} + E_i + E_j)/RT]\theta_C{}^2(\theta_H/\theta_*)^{i+j} \quad (13)$$

where A, $E_{a,i+j}$, θ_{CHi}, θ_{CHj}, θ_C, θ_H, and θ_* are the pre-exponential factor, the reaction barrier for $Ch_i + CH_j$ coupling, the coverage of CH_i, CH_j, C, H and the free site, respectively. The effective barrier of the coupling of $CH_i + CH_j$ ($E_{a\_eff,i+j}$) is equal to $E_{a,i+j} + E_i + E_j$, where E_i and E_j are the reaction energies for C + iH → CH_i and C + jH → CH_j, respectively.

In the CO-insertion mechanism, the CO + CH_j coupling rate is expressed as

$$r_{CO_i+CH_j} = A\exp[-E_{a,CO+j}/RT]P_{CO}\theta_{CHj} = A\exp[-(E_{a,CO+j} + E_j)/RT]P_{CO}\theta_C(\theta_H/\theta_*)^j \quad (14)$$

where P_{CO} is the pressure of CO. The effective barrier of the coupling of CO + CH_j ($E_{a\_eff,CO+j}$) is $E_{a,CO+Ej}$, where E_j is the reaction energy for the C + jH → CH_j.[38,41,44,72]

It turns out that the coupling of $CH_i + CH_j$, and CH_i + CO on ten cobalt surfaces resembles each other, and we hereby use the hcp-Co (0001) surface as an example to demonstrate the most feasible $C_1 + C_1$ coupling reaction. The energy profiles of the $C_1 + C_1$ coupling reaction on hcp-Co (0001) are shown in Fig. 4. The $E_{a\_eff,i+j}$ of C + CH (0.41 eV), C + CH_2 (0.86 eV), and C + CH_3 (1.28 eV) gradually increase with the hydrogenation of the carbon atom, indicating that the coupling ability of carbon species will be reduced, due to the increase of the coordination number of the C atom. A similar increasing trend of $E_{a\_eff,+j}$ is observed for CH + CH (0.10 eV), CH + CH_2 (0.52 eV), and CH + CH_3 (1.38 eV).

We take the hcp-Co (0001) as an example to discuss the $C_1 + C_1$ coupling reaction. Since CH_4 formation competes with $C_1 + C_1$ coupling, if the barrier of a particular $C_1 + C_1$ coupling reaction is higher than CH_4 formation, then the C1 species will be directly hydrogenated and this $C_1 + C_1$ coupling reaction will not be likely to happen. We found that the carbide mechanisms of C + C, C + CH, C + CH_2, CH + CH, CH + CH_2 reactions are all feasible on hcp-Co (0001), due to their lower $E_{a\_eff,i+j}$ than E_{a_eff,CH_4}. However, the CO-insertion mechanism of C + CO, CH + CO, CH_2 + CO, and CH_3 + CO coupling reaction all has higher $E_{a\_eff,CO+j}$ than E_{a_eff,CH_4}, indicating that the CO-insertion mechanisms are not favorable on hcp-Co (0001). Among the feasible carbide mechanisms, the CH + CH coupling has the

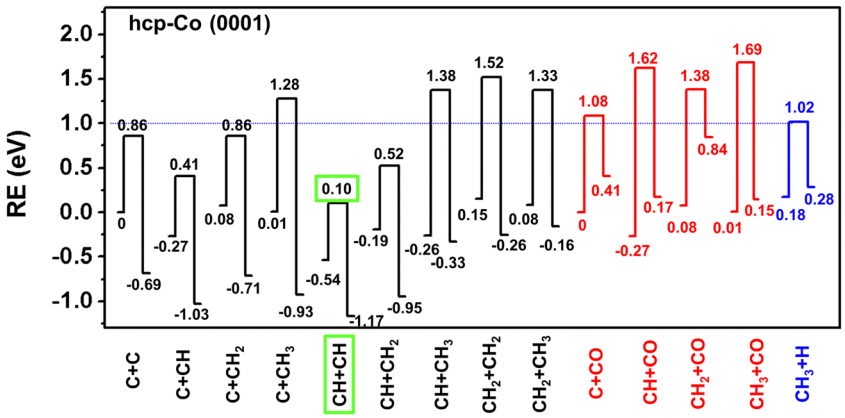

Fig. 4 Energy profiles of the carbide mechanism, the CO-inserted mechanism and the CH_4 formation on hcp-Co (0001) model surfaces. The energy of $E_i + E_j$ is chosen as the zero point. (The blue dotted line is the effective barrier of CH_4 formation. The green rectangle is the most feasible pathway of the $C_1 + C_1$ coupling reaction and the related effective barrier.).

lowest $E_{a\_eff,i+j}$, and is probably the most favorable pathway among all the $C_1 + C_1$ coupling reactions on the hcp-Co (0001) surface.[45]

For the other hcp-Co and fcc-Co surfaces, the most feasible $C_1 + C_1$ coupling pathways are divergent. It is CH + CH on hcp-Co (10−10), (10−12), (11−21), fcc-Co (110), (111), C + CH_3 on fcc-Co (311), C + CO on hcp-Co (10−11), fcc-Co (100), and CH + CO on hcp-Co (11−20), as shown in Table 1 and Fig. S13 (ESI†). For most of the surfaces, the reaction of CH + CH coupling is the most favorable pathway among all of the $C_1 + C_1$ coupling reactions, which is in line with the findings in ref. 44 and 73.

3.3 CH_4 selectivity

As Cheng[42,72] and Yin, *et al.*[41] have proven, the CH_4 selectivity in FTS can be approximately evaluated based on the effective barrier difference of CH_4 formation and $C_1 + C_1$ coupling.: $\Delta E_{a\_eff} = E_{a\_eff,CH_4} - E_{a\_eff,C_1+C_1}$, where E_{a_eff,CH_4} is the effective barrier of CH_4 formation, and E_{a_eff,C_1+C_1} is the effective barrier of the most feasible $C_1 + C_1$ coupling. The CH_4 selectivity is thus negatively associated with the value of ΔE_{a_eff} (Fig. 5).

It is worth noting that the CH_4 selectivity in hcp is not always lower than in fcc. Among the ten Co surfaces, hcp-Co (10−10) has the largest ΔE_{a_eff} (2.13 eV), indicating the lowest CH_4 selectivity, whereas fcc-Co (311) has the smallest ΔE_{a_eff} (0.55 eV) and the highest CH_4 selectivity. However, the ΔE_{a_eff} values of hcp-Co (0001), (10−12), and (11−20) are even lower than those of fcc-Co (100) and fcc-Co (111), implying higher CH_4 selectivity of these surfaces on hcp-Co. The ranks of the CH_4 selectivity of all the Co surfaces are shown in Fig. 5. To confirm the validity of our prediction, comparisons are made with the available experiments. Qin *et al.* have synthesized three types of hcp-Co particles

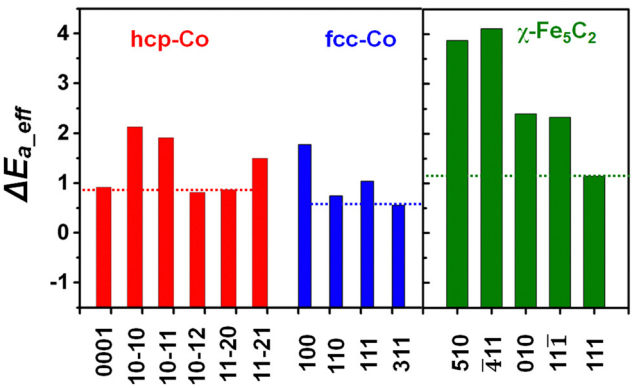

Fig. 5 The effective barrier difference ($\Delta E_{a\_eff} = E_{a\_eff,CH_4} - E_{a\_eff,C_1+C_1}$, the columns) and the particle effective barrier difference ($\Delta E_{a\_particle}$, the dashed lines) between CH_4 formation and the most feasible $C_1 + C_1$ coupling on hcp-Co (0001), (10−10), (10−11), (10−12), (11−20), (11−21), fcc-Co (100), (110), (111), (311), and Fe_5C_2 (510), ($\bar{4}$11), (010), (11$\bar{1}$), (111). The ΔE_{a_eff} of Fe_5C_2 (510), ($\bar{4}$11), (010), (11$\bar{1}$), (111) is from ref. 36.

exposing only one type of facet each. Comparison of their CH_4 selectivity shows that (10−11) has the lowest CH_4 selectivity, followed by (0001) and (11−20). Our calculated ΔE_{a_eff} values on (10−11), (0001), and (11−20) are 1.92 eV, 0.92 eV, and 0.87 eV, respectively, with the rank of CH_4 selectivity to be (10−11) < (0001) < (11−20), which is in excellent agreement with the experiments.[68]

The overall CH_4 selectivities of hcp-Co and fcc-Co phases are defined by the particle effective barrier difference ($\Delta E_{a\_particle}$) between CH_4 formation (E_{a_eff,CH_4}) and the most feasible $C_1 + C_1$ coupling (E_{a_eff,C_1+C_1}) on hcp-Co and fcc-Co Wulff particles,

Table 1 The most feasible pathway of the $C_1 + C_1$ coupling reaction and the related effective barrier on hcp-Co (0001), (10−10), (10−11), (10−12), (11−20), (11−21) and fcc-Co (100), (110), (111), (311) model surfaces

	(10−10)	(10−11)	(10−12)	(11−20)	(11−21)	(100)	(110)	(111)	(311)
$C_1 + C_1$	CH + CH	C + CO	CH + CH	CH + CO	CH + CH	C + CO	CH + CH	CH + CH	C + CH_3
$E_{a\_eff,i+j}/E_{a\_eff,CO+j}$	0.05	1.42	1.21	0.18	0.67	1.05	0.20	−0.01	0.77

assuming that the overall rate of reaction on the catalyst particle is the sum of the rates from all its exposed surfaces. (See the Methods section). The $\Delta E_{a\_particle}$ on hcp-Co and fcc-Co surfaces is 0.86 eV and 0.60 eV, respectively. Therefore, the CH_4 selectivity in FTS is higher on fcc-Co than on hcp-Co, which is consistent with the experimental observations.[33,74,75] Notably, the (311) surface of fcc-Co plays a pivotal role in determining the overall CH_4 selectivity of the fcc phase. Moreover, our results suggest that the CH_4 selectivity can be suppressed by decreasing the exposure ratio of the facets that are prone to form CH_4: (0001), (10−12), and (11−20) on hcp-Co and (110) and (311) on fcc-Co.

In FTS, Co-based FTS generally has higher CH_4 selectivity than Fe-based FTS.[42,76] Herein, we compare the ΔE_{a_eff} of exposed facets of hcp and fcc Co with those of χ-Fe_5C_2 particles,[36] the most widely accepted active phase in iron-catalyzed FTS.[11,23,37] Most of the χ-Fe_5C_2 surfaces have large ΔE_{a_eff}, with the exception of Fe_5C_2(111), which has lower ΔE_{a_eff} than the cobalt surfaces of (10−10), (10−11), (11−21), and (100). The overall CH_4 selectivity of χ-Fe_5C_2, hcp-Co, and fcc-CO can be compared using $\Delta E_{a\_particle}$ (Fig. 5, dashed lines and Table S9, ESI†). The $\Delta E_{a\_particle}$ (1.20 eV) of Fe_5C_2 particles is larger than that of hcp-Co and fcc-Co, indicating that the Co particle of both phases has higher CH_4 selectivity than the χ-Fe_5C_2 particle. This is probably the reason why Co-based FTS generally shows higher CH_4 selectivity than Fe-based FTS.[41]

3.4 Tuning of the phase transition between hcp and fcc Co

On the basis of the understanding of the activity and selectivity for CH_4 and C_{2+} production on the cobalt phases, one can further use the knowledge for catalyst design through phase engineering. Operando characterization shows that in FTS, the cobalt catalyst can exist in both hcp and fcc phases.[77,78] In order to get more hcp phase which has lower CH_4 selectivity and higher C_{5+} selectivity, the thermodynamic conditions for the modulation of the ratio of hcp and fcc Co phases by changing the temperature and particle size are explored.

The thermodynamic stability of the Co particles of different phases can be evaluated using the Gibbs free energy per cobalt atom, which involves the energy, phonon energies at certain temperature, and surfaces energies at a given particle size.[55–58] The details of the theory and calculation methods are shown in Section 2.4. The temperature and particle sizes in which the Gibbs free energy difference is zero represent the condition of phase transition between hcp-Co and fcc-Co, which is given in Fig. 6 and Table S10 (ESI†). The black solid curve corresponds to the conditions of phase transition of bulk cobalt. At 718 K, a phase transition from hcp-Co to fcc-Co happens, which is very close to the experimental transition temperature of 695 K.[79,80] This shows that bulk hcp-Co is more stable than bulk fcc-Co below 718 K, and keeping a low operating temperature (<718 K) is beneficial for stabilizing the hcp-Co phase. On the other hand, the particle size also plays an important role in the phase transition as shown in Fig. 6. The transition temperatures of different particle sizes (10 nm, 15 nm, 20 nm, 25 nm, and 30 nm) are 1059 K, 946 K, 890 K, 855 K, and 833 K, respectively. With the increase in the size of cobalt particles, the phase transition temperature gradually decreases until it approaches the bulk transition temperature. When the particle size is larger than 30 nm, hcp-Co is stable only at a relatively narrow temperature window between 718 K and 833 K. Therefore, the ratio of hcp phase particles could be maximized by controlling the operating temperature below 718 K and size of the Co particles as small as possible within the range of 10–30 nm, which will likely lower CH_4 selectivity and improve C_{5+} selectivity of the FTS process as observed experimentally.[81]

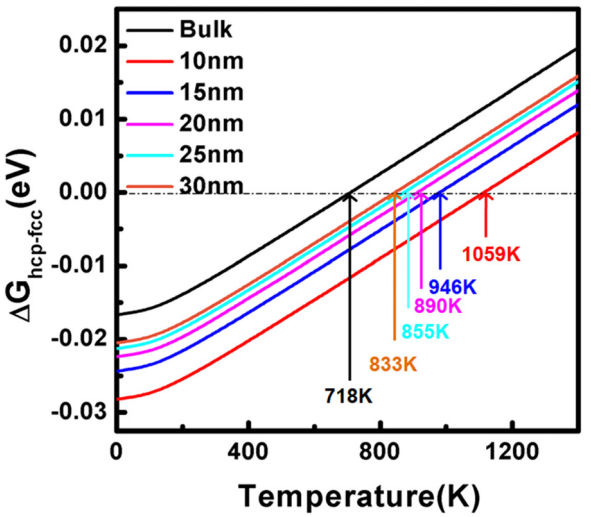

Fig. 6 Calculated Gibbs free energy difference for hcp-Co and fcc-Co phases as a function of temperature at different particle sizes.

4. Conclusion

In this work, we proposed a strategy combining DFT, Wulff construction, and a particle-level energy descriptor to understand the relationship between the crystal phase and their catalytic selectivity, using the CH_4 formation on hcp-Co and fcc-Co as an example. Hcp-Co has lower intrinsic catalytic activity than fcc-Co to form CH_4, due to the higher $E_{a\_particle,CH_4}$. A linear relationship was discovered between E_{a_eff,CH_4} of a Co surface and the sum of adsorption energies of a C atom and 4H atoms on it (E_{ads_C+4H}), which provides an efficient way of predicting the intrinsic catalytic activity of Co surfaces for CH_4 formation. The most feasible $C_1 + C_1$ coupling pathway is CH + CH on hcp-Co (0001), (10−10), (10−12), (11−21), fcc-Co (110), (111), C + CH_3 on fcc-Co (311), C + CO on hcp-Co (10−11), fcc-Co (100), and CH + CO on hcp-Co (11−20). The CH_4 selectivity, represented by the effective barrier difference between CH_4 formation and the most feasible $C_1 + C_1$ coupling, decreases in the sequence of surfaces (311) > (110) > (10−12) > (11−20) > (0001) > (111) > (11−21) > (100) > (10−11) > (10−10). The lower CH_4 selectivity of hcp-Co than fcc-Co can be well explained by its higher $\Delta E_{a\_particle}$. Tuning the CH_4 selectivity of the Co catalyst can be achieved not only by controlling the morphology of the particles to avoid the active facets for CH_4 formation such as (0001), (10−12), (11−20) on hcp-Co and

(110), (311) on fcc-Co, but is also achievable through engineering the crystal phases by controlling the temperature and particle size. Our research provides a pathway to understand the phase-selectivity relationship for complex reactions.

Conflicts of interest

There are no conflicts to declare.

Acknowledgements

The authors are grateful for the financial support from the National Science Fund for Distinguished Young Scholars of China (Grant no. 22225206), the National Key R&D Program of China (2022YFA1604103), the National Natural Science Foundation of China (No. 21972160, 21972157, 22372187), CAS Project for Young Scientists in Basic Research (YSBR-005), Key Research Program of Frontier Sciences CAS (ZDBS-LY-7007), Major Research plan of the National Natural Science Foundation of China (92045303), Informatization Plan of Chinese Academy of Sciences, (Grant no. CAS-WX2021SF0110), Youth Innovation Promotion Association CAS (2020179), the Doctoral Research Funds in Shanxi (QZX-2023012), the Scientific and Technological Innovation Programs of Higher Education Institutions in Shanxi (2023L304), the Doctoral Research Funds of Yuncheng University (YQ2023025), and the Autonomous Research Project of SKLCC (Grant no. 2023BWZ005).

References

1 Y. Liu and W. E. Mustain, *J. Am. Chem. Soc.*, 2013, **135**, 530–533.
2 Y. Jiao, T. Chen, L. Wang, P. Yao, J. Zhang, Y. Chen, Y. Chen and J. Wang, *Ind. Eng. Chem. Res.*, 2020, **59**, 4338–4347.
3 W. Shafer, M. Gnanamani, U. Graham, J. Yang, C. Masuku, G. Jacobs and B. Davis, *Catalysts*, 2019, **9**, 259.
4 E. Iglesia, *Appl. Catal., A*, 1997, **161**, 59–78.
5 J. H. den Otter, S. R. Nijveld and K. P. de Jong, *ACS Catal.*, 2016, **6**, 1616–1623.
6 V. Subramanian, K. Cheng, C. Lancelot, S. Heyte, S. Paul, S. Moldovan, O. Ersen, M. Marinova, V. V. Ordomsky and A. Y. Khodakov, *ACS Catal.*, 2016, **6**, 1785–1792.
7 L. Zhang, Y. Dang, X. Zhou, P. Gao, A. P. van Bavel, H. Wang, S. Li, L. Shi, Y. Yang, E. I. Vovk, Y. Gao and Y. Sun, *Innovation*, 2021, **2**, 100170.
8 Ø. Borg, N. Hammer, B. C. Enger, R. Myrstad, O. A. Lindvåg, S. Eri, T. H. Skagseth and E. Rytter, *J. Catal.*, 2011, **279**, 163–173.
9 E. Rytter, N. E. Tsakoumis and A. Holmen, *Catal. Today*, 2016, **261**, 3–16.
10 S. Rane, Ø. Borg, E. Rytter and A. Holmen, *Appl. Catal., A*, 2012, **437–438**, 10–17.
11 T. A. Wezendonk, X. Sun, A. I. Dugulan, A. J. F. van Hoof, E. J. M. Hensen, F. Kapteijn and J. Gascon, *J. Catal.*, 2018, **362**, 106–117.
12 P. Wang, W. Chen, F. K. Chiang, A. I. Dugulan, Y. Song, R. Pestman, K. Zhang, J. Yao, B. Feng, P. Miao, W. Xu and E. J. M. Hensen, *Sci. Adv.*, 2018, **4**, eaau2947.
13 W. Chen, Z. Fan, X. Pan and X. Bao, *J. Am. Chem. Soc.*, 2008, **130**, 9414–9419.
14 Q. Zhang, J. Kang and Y. Wang, *ChemCatChem*, 2010, **2**, 1030–1058.
15 W. Li, J. Liu, J. Gu, W. Zhou, S. Yao, R. Si, Y. Guo, H. Su, C. Yan, W. Li, Y. Zhang and D. Ma, *J. Am. Chem. Soc.*, 2017, **139**, 2267–2276.
16 H. Tian, X. Li, L. Zeng and J. Gong, *ACS Catal.*, 2015, **5**, 4959–4977.
17 E. de Smit, F. Cinquini, A. M. Beale, O. V. Safonova, W. van Beek, P. Sautet and B. M. Weckhuysen, *J. Am. Chem. Soc.*, 2010, **132**, 14928–14941.
18 D. Luo, X. C. Liu and R. Gao, *et al.*, *J. Phys. Chem. C*, 2020, **124**, 18576–18586.
19 O. Kitakami, H. Sato, Y. Shimada, F. Sato and M. Tanaka, *Phys. Rev. B: Condens. Matter Mater. Phys.*, 1997, **56**, 13849–13854.
20 N. Fischer, E. van Steen and M. Claeys, *Catal. Today*, 2011, **171**, 174–179.
21 L. Zhong, F. Yu, Y. An, Y. Zhao, Y. Sun, Z. Li, T. Lin, Y. Lin, X. Qi, Y. Dai, L. Gu, J. Hu, S. Jin, Q. Shen and H. Wang, *Nature*, 2016, **538**, 84–87.
22 V. Lyaskovskyy and B. de Bruin, *ACS Catal.*, 2012, **2**, 270–279.
23 R. Nakano, L. W. Chung, Y. Watanabe, Y. Okuno, Y. Okumura, S. Ito, K. Morokuma and K. Nozaki, *ACS Catal.*, 2016, **6**, 6101–6113.
24 Z. Li, S. Ji, Y. Liu, X. Cao, S. Tian, Y. Chen, Z. Niu and Y. Li, *Chem. Rev.*, 2020, **120**, 623–682.
25 X. Zhang, R. A. van Santen and E. J. M. Hensen, *ACS Catal.*, 2014, **5**, 596–601.
26 G. Sun and P. Sautet, *J. Am. Chem. Soc.*, 2018, **140**, 2812–2820.
27 Z. Zhang, B. Zandkarimi and A. N. Alexandrova, *Acc. Chem. Res.*, 2020, **53**, 447–458.
28 P. Ann Lin, B. Natarajan, M. Zwolak and R. Sharma, *Nanoscale*, 2018, **10**, 4528–4537.
29 M. S. Spencer, *Nature*, 1986, **323**, 685–687.
30 Y. Chen, Z. Fan, J. Wang, C. Ling, W. Niu, Z. Huang, G. Liu, B. Chen, Z. Lai, X. Liu, B. Li, Y. Zong, L. Gu, J. Wang, X. Wang and H. Zhang, *J. Am. Chem. Soc.*, 2020, **142**, 12760–12766.
31 J. Cao, J. Xia, Y. Zhang, X. Liu, L. Bai, J. Xu, C. Yang, S. Zheng, T. Yang, K. Tang, C. Zhang and C. Zhou, *Fuel*, 2021, **289**, 119843.
32 J. F. Gómez-García, J. A. Mendoza-Nieto, A. Yañez-Aulestia, F. Plascencia-Hernández and H. Pfeiffer, *Fuel Process. Technol.*, 2020, **204**, 106404.
33 M. K. Gnanamani, G. Jacobs, W. D. Shafer and B. H. Davis, *Catal. Today*, 2013, **215**, 13–17.
34 H. Du, M. Jiang, H. Zhu, C. Huang, Z. Zhao, W. Dong, W. Lu, T. Liu, Z. Conrad Zhang and Y. Ding, *Fuel*, 2021, **292**, 120244.
35 L. Zhong, Doctoral thesis, Nanyang Technological University, Singapore, 2020.

36 M. Armbruster, K. Kovnir,M. Behrens, D. Teschner, Y. Grin and R. Schlogl, *J. Am. Chem. Soc.*, 2010, **132**, 14745–14747.
37 J. Yin, X. Liu, X. Liu, H. Wang, H. Wan, S. Wang, W. Zhang, X. Zhou, B. Teng, Y. Yang, Y. Li, Z. Cao and X. Wen, *Appl. Catal., B*, 2020, **278**, 119308.
38 T. H. Pham, Y. Qi, J. Yang, X. Duan, G. Qian, X. Zhou, D. Chen and W. Yuan, *ACS Catal.*, 2015, **5**, 2203–2208.
39 G. P. van der Laan and A. A. C. M. Beenackers, *Catal. Rev.: Sci. Eng.*, 1999, **41**, 255–318.
40 M. E. Dry, *Catal. Today*, 2002, **71**, 227–241.
41 J. Yin, Y. He, X. Liu, X. Zhou, C. F. Huo, W. Guo, Q. Peng, Y. Yang, H. Jiao, Y. W. Li and X. D. Wen, *J. Catal.*, 2019, **372**, 217–225.
42 J. Cheng, P. Hu, P. Ellis, S. French, G. Kelly and C. M. Lok, *J. Phys. Chem. C*, 2009, **113**, 8858–8863.
43 X. Q. Gong, R. Raval and P. Hu, *J. Chem. Phys.*, 2005, **122**, 024711.
44 M. Yu, L. Liu, Q. Wang, L. Jia, J. Wang, D. Li and B. Hou, *J. Phys. Chem. C*, 2020, **124**, 11040–11049.
45 J. Cheng, X. Gong, P. Hu, C. Lok, P. Ellis and S. French, *J. Catal.*, 2008, **254**, 285–295.
46 P. Zhao, Z. Cao, X. Liu, P. Ren, D. Cao and H. Xiang, *et al.*, *ACS Catal.*, 2019, **9**, 2768–2776.
47 G. Kresse and J. Furthmüller, *Comput. Mater. Sci.*, 1996, **6**, 15–50.
48 G. Kresse and J. Furthmüller, *Phys. Rev. B: Condens. Matter Mater. Phys.*, 1996, **54**, 11169–11186.
49 P. E. Blöchl, *Phys. Rev. B: Condens. Matter Mater. Phys.*, 1994, **50**, 17953–17979.
50 G. Kresse and D. Joubert, *Phys. Rev. B: Condens. Matter Mater. Phys.*, 1999, **59**, 1758–1775.
51 J. P. Perdew, K. Burke and M. Ernzerhof, *Phys. Rev. Lett.*, 1996, **77**, 3865–3868.
52 M. Methfessel and A. T. Paxton, *Phys. Rev. B: Condens. Matter Mater. Phys.*, 1989, **40**, 3616–3621.
53 G. Henkelman and H. Jónsson, *J. Chem. Phys.*, 2000, **113**, 9978–9985.
54 D. Lide and H. Kehiaian, *CRC Handbook of Chemistry and Physics*, CRC Press, BocaRaton, FL, 1994.
55 J. X. Liu, H. Y. Su and W. X. Li, *Catal. Today*, 2013, **215**, 36–42.
56 J. Häglund, A. Fernández Guillermet, G. Grimvall and M. Körling, *Phys. Rev. B: Condens. Matter Mater. Phys.*, 1993, **48**, 11685–11691.
57 W. Luo and A. Asthagiri, *J. Phys. Chem. C*, 2014, **118**, 15274–15285.
58 B. Böller, K. M. Durner and J. Wintterlin, *Nat. Catal.*, 2019, **2**, 1027–1034.
59 C. J. K. Weststrate, D. Sharma, D. Garcia Rodriguez, M. A. Gleeson, H. O. A. Fredriksson and J. W. H. Niemantsverdriet, *Nat. Commun.*, 2020, **11**, 750.
60 G. F. Wei and Z. P. Liu, *Chem. Sci.*, 2015, **6**, 1485–1490.
61 G. J. Kaptay, *Nanosci. Nanotechnol.*, 2012, **12**, 2625–2633.
62 N. Wu, X. Ji, R. An, C. Liu and X. Lu, *AIChE J.*, 2017, **63**, 4595–4603.
63 B. Singh, M. K. Gupta, R. Mittal and S. L. Chaplot, *Phys. Chem. Chem. Phys.*, 2018, **20**, 12248–12259.
64 A. Navrotsky, C. Ma, K. Lilova and N. Birkner, *Science*, 2010, **330**, 199–201.
65 A. Togo, F. Oba and I. Tanaka, *Phys. Rev. B: Condens. Matter Mater. Phys.*, 2008, **78**, 134106.
66 A. Navrotsky, *ChemPhysChem*, 2011, **12**, 2207–2215.
67 C. Chen, Q. Wang, G. Wang, B. Hou, L. Jia and D. Li, *J. Phys. Chem. C*, 2016, **120**, 9132–9147.
68 C. Qin, B. Hou, J. Wang, Q. Wang, G. Wang, M. Yu, C. Chen, L. Jia and D. Li, *ACS Catal.*, 2018, **8**, 9447–9455.
69 J. Cheng, P. Hu, P. Ellis, S. French, G. Kelly and C. M. Lok, *J. Phys. Chem. C*, 2010, **114**, 1085–1093.
70 F. Fischer and H. Tropsch, *Brennst. Chem.*, 1926, **7**, 97–104.
71 H. Pichler and H. Schulz, *Chem. Ing. Tech.*, 1970, **12**, 1160–1174.
72 J. Cheng, P. Hu, P. Ellis, S. French, G. Kelly and C. M. Lok, *J. Phys. Chem. C*, 2008, **112**, 6082–6086.
73 P. Zhai, P. Chen and J. Xie, *et al.*, *Faraday Discuss.*, 2017, **197**, 207–224.
74 G. Xiao, J. Yan, J. Du, Y. Han, F. Sun, Y. Zhang, J. Li and J. Hong, *Fuel*, 2019, **254**, 115577.
75 L. Nie, Z. Li, T. Kuang, S. Lyu, S. Liu, Y. Zhang, B. Peng, J. Li and L. Wang, *Chem. Commun.*, 2019, **55**, 10559–10562.
76 W. Ma, G. Jacobs, D. E. Sparks, B. Todic, D. B. Bukur and B. H. Davis, *Catal. Today*, 2020, **343**, 125–136.
77 L. J. Garces, B. Hincapie, R. Zerger and S. L. Suib, *J. Phys. Chem. C*, 2015, **119**, 5484–5490.
78 H. Karaca, J. Hong, P. Fongarland, P. Roussel, A. Griboval-Constant, M. Lacroix, K. Hortmann, O. V. Safonova and A. Y. Khodakov, *Chem. Commun.*, 2010, **46**, 788–790.
79 T. Nishizawa and K. Ishida, *Bull. Alloy Phase Diagrams*, 1983, **4**, 387–390.
80 J. Sort, J. Nogués, S. Suriñach, J. S. Muñoz and M. D. Baró, *Mater. Sci. Eng., A*, 2004, **375–377**, 869–873.
81 G. L. Bezemer, J. H. Bitter, H. P. Kuipers, H. Oosterbeek, J. E. Holewijn, X. Xu, F. Kapteijn, A. J. van Dillen and K. P. De Jong, *J. Am. Chem. Soc.*, 2006, **128**, 3956–3964.

